Three-Dimensional Forward Modeling of Ground Wire Source Transient Electromagnetic Data Using the Meshless Generalized Finite Difference Method

Tianjiao Li, Ming Zhang, and Jun Lin

***Abstract*— The transient electromagnetic (TEM) method is a geophysical exploration method commonly used in the detection of subsurface structures. Underground conductivity information at different depths can be obtained by interpreting the observed time-varying TEM data. Three-dimensional forward modeling is important for studying TEM responses and is also essential for inversion. The calculation accuracy of mesh-based forward modeling methods, such as the finite volume method (FVM) and finite-element method (FEM), is greatly affected by the quality of the mesh. In this article, a TEM forward modeling method based on a meshless generalized finite difference method (GFDM) is proposed. It is based on the Taylor expansion and weighted least squares fitting. In the GFDM, a partial derivative of the unknown parameter in the governing equation is expressed as a linear combination of the function values of support points. Numerical integration is not required during the forward modeling process, which simplifies the program implementation and increases the numerical calculation efficiency. In this article, a 3-D GFDM forward modeling method for simulating ground wire source TEM data is investigated; a corresponding program is developed, and the correctness of the code is verified through several 3-D models. By comparing the forward modeling results of this method with those of the FEM, it is verified that the GFDM offers higher computational speed and lower memory requirements.**

***Index Terms*— 3-D forward modeling, generalized finite difference method (GFDM), transient electromagnetic (TEM) method, wire source.**

I. Introduction

THE transient electromagnetic (TEM) method energizes electrically conducting earth using a line source or a loop of wire and measures the TEM responses over many receiver sites to obtain subsurface electrical resistivity [1], [2], [3]. It has advantages of relatively good measurement efficiency and relatively low survey costs. Because of this, it has been widely used in many geophysical prospecting scenarios, such as investigating underground geological structures and exploring mineral and groundwater sources [4], [5], [6], [7], [8].

Accurate and efficient 3-D forward modeling is the basis for electromagnetic response characteristic analysis and is also a prerequisite for inversion interpretation [9], [10]. The integral equation method, finite difference method (FDM), finite volume method (FVM), and finite-element method (FEM) have successively become mainstream methods for the forward modeling of EM data [9], [11], [18], [19]. The integral equation method was favored in earlier days because it only required the calculation of a field in a small volume anomaly domain, and the memory requirements were low [12], [13], [14]. With the increase in memory and processing speed of computers, the FDM, FEM, and FVM have been followed with interest in recent decades. Therein, the FDM is a method that uses discrete difference operators based on a Taylor series to approximate the continuous differential operators in a partial differential equation. When using the FDM, the solution domain is generally divided into a staggered grid, and the unknowns of magnetic field components and electric field components are placed at the center of cell faces and in the middle of cell edges, respectively [9], [16], [15]. Although the FDM can be used in 3-D electromagnetic forward modeling, there are limitations in the forward modeling of complex realistic geological models. In recent years, the FVM and the FEM have drawn more attention because of their flexibility in unstructured mesh generation [17], [18]. By using an unstructured mesh, local refinement can be easily carried out, which results in fewer numbers of freedoms to be solved. Less computing time is therefore consumed, and less computer memory usage is required [19], [20]. To make the best use of the unstructured mesh, open-source software programs, such as TetGen and FacetModeller, have been developed and are available for free, which also advances the development of the FVM and FDM [21], [22], [23]. These attractive features lead to their important role in the forward modeling of arbitrary real-life 3-D models [24], [25].

At present, total field forward modeling algorithms and secondary field forward modeling algorithms predominate for 3-D forward simulations of controlled source electromagnetic field data, both of which have their own advantages. The advantage of the total field forward modeling algorithm is that it directly calculates the total field response of the electromagnetic field at any position without the need to consider the primary field of the background model; hence, it is highly applicable to complex models. However, as the electromagnetic field

Manuscript received 29 November 2022; revised 23 June 2023; accepted 1 July 2023. Date of publication 4 July 2023; date of current version 25 July 2023. This work was supported in part by the National Natural Science Foundation of China under Grant 42204151, Grant 41827803, and Grant 42074152. *(Corresponding author: Ming Zhang.)*

Tianjiao Li is with the Changchun Institute of Optics, Fine Mechanics and Physics, Chinese Academy of Science, Changchun 130033, China, also with the School of Optoelectronics, University of Chinese Academy of Sciences, Beijing 100049, China, and also with the College of Instrumentation and Electrical Engineering, Jilin University, Changchun 130021, China (e-mail: litj@ciomp.ac.cn).

Ming Zhang and Jun Lin are with the College of Instrumentation and Electrical Engineering, Jilin University, Changchun 130021, China, and also with the Key Laboratory of Geophysical Exploration Equipment, Ministry of Education of China, Jilin University, Changchun 130000, China (e-mail: zhangming2020@jlu.edu.cn; linjun@jlu.edu.cn).

Digital Object Identifier 10.1109/TGRS.2023.3292294

response near the source varies drastically, a smaller mesh is required to simulate this variation more accurately. This results in many freedoms and high consumption of computational time and memory [26], [27], [28], [29]. In contrast, although the secondary field algorithm needs to find a proper background model and calculate the responses of such a model, it does not require refining the mesh near the source, hence resulting in less freedom and computational time [30], [31].

The boundary condition is a significant factor that influences the numerical accuracy of electromagnetic data forward modeling. The Dirichlet boundary condition, which assumes a zero value of the electric or magnetic field at the outer boundaries, can be applied if the boundaries are sufficiently far away from the area of interest. The perfectly matched layer (PML) boundary condition, which uses a few absorbing layers around the area of interest to depress the artificial boundary effect, is another option. By using it, the computation domain can be restricted to the target region, which can shorten the computation time and reduce the memory requirement [32], [33], [34], [35], [36].

The abovementioned forward modeling methods, such as the FEM and FVM, are mesh-based methods, and the quality of the mesh, e.g., the shape of the cell, has a significant influence on the computational accuracy. In recent years, the application of a meshless method to geophysical electromagnetic forward modeling has been investigated. By using meshless methods, the computational domain is generated into a set of unconnected points rather than meshes. Meshless local petrov-galerkin method (MLPG), radial point interpolation method (RPIM), and radial basis function (RBF)-based methods are typical meshless methods that can be used to solve electromagnetic problems [37], [38], [39]. In this article, we investigate another type of meshless method, i.e., the meshless generalized FDM (GFDM), which is a strong-form-based meshless method [40], [41], [42]. It introduces the concept of point clusters and expresses the function values at the central point by a linear combination of the function values of the support points and that of the central point. One of the advantages of the GFDM over mesh-based methods (i.e., FD, FV, and FE methods) is that the discretization of points is more straightforward and more robust than the generation of quality meshes. This helps overcome the aforementioned challenges in the representation of models with overly complex geometry when using mesh-based methods. In addition, as a connection between points is not needed, adding or deleting some points will not affect the rest, which makes it easy and more efficient to conduct adaptive refinement of the discretization than using the mesh-based methods. It also provides the basis for adaptive inversion. Furthermore, since the GFDM solves the strong-form partial differential equations, the basis function and numerical integration are not needed, and it can therefore effectively prevent the interpolation difficulties caused by mesh distortion in regions with complex geometry. This can also make the derivative calculation more accurate and efficient, as losing accuracy and increasing computation time during the integration computation procedure can be avoided. Moreover, the coefficient matrix generated by the GFDM is a sparse matrix similar to that in the FEM; hence, the GFDM linear equation system for the TEM problem can be easily and quickly solved by either direct or iterative solvers. In this article, the system is solved using a direct solver [27], [30], [31].

Because of the abovementioned advantages, the GFDM has been applied to the forward modeling of several engineering problems, but its application to a 3-D wire source TEM problem by solving the E-field equations has not yet been widely reported [44], [45]. The limitation of this application lies in the following two main problems that need to be solved.

For the TEM problem considered in this article, as an electrical wire source is applied, the source term in the linear equation system needs to be mathematically handled. When solving the problem using the FEM and FVM, this is generally conducted by treating the density of the current as a pseudo-δ function. However, such handling is not applicable in the GFDM. The reasons are given as follows. In the FEM and FVM, the spatial integral of the pseudo-δ function is determined, which results in a constant value. In the GFDM, the integral is not needed, and the direct use of such a pseudo-δ function would result in an infinite value that is unusable in the numerical calculation. To solve the abovementioned problem, we deduced the GFDM linear equation system based on the secondary E-field of the wire source TEM problem. The derivation details of the equation are given in Section II.

Another problem is that the GFDM approximation of the unknown function constructed for the TEM problem is of high-order continuity (the derivation details of the GFDM approximation are given in Sections III and IV), which is in violation of the discontinuous normal component requirement for the E-field at the interface. Unlike the FE method, in which the discontinuity of conductivity is explicitly present in the mesh, in the GFDM, the discontinuities are not presented in the cloud of points. Therefore, it is challenging for the GFDM to reproduce the discontinuity. To solve this problem, we imposed inner interface conditions and conducted special conductivity assignments for the interface points. The details are introduced in Section V.

In this article, a 3-D forward simulation method of ground wire source TEM data based on the GFDM is studied, and a corresponding program is developed. Forward modeling and analysis of the TEM response of typical 3-D models are carried out, and the calculation results are compared with those of the FEM. We also investigate the computational efficiency and memory usage of the GFDM by comparing these parameters with those of the FEM under the same discretization (i.e., the distribution of the points of the GFDM is the same as the distribution of mesh vertices in the FEM).

II. Secondary E-Field Equations for the TEM Problem

In this article, we considered a TEM configuration with a grounded wire source. The schematic of the 3-D geoelectric model is shown in Fig. 1.

The Maxwell equations in the time domain [10], [12], [15] are given by

$$\nabla \times \boldsymbol{E} = -\mu_0 \frac{\partial \boldsymbol{H}}{\partial t} \tag{1}$$

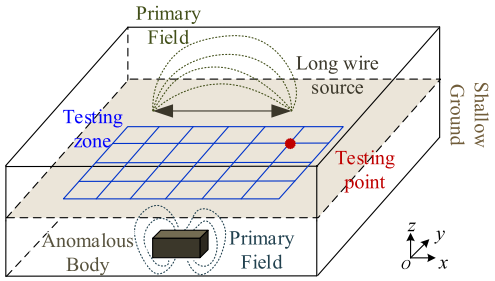

Fig. 1. Schematic of the principle of time-domain electromagnetic detection.

$$\nabla \times \boldsymbol{H} = \sigma \boldsymbol{E} + \boldsymbol{J_s} \tag{2}$$

where E denotes the electric field, H denotes the magnetic field, t denotes the time, σ denotes the dielectric conductivity, μ_0 denotes the permeability of the vacuum, and CCC denotes the source current density. Taking the rotation at both ends of (1) yields the following equation:

$$\nabla \times \nabla \times \boldsymbol{E} = -\mu_0 \frac{\partial \nabla \times \boldsymbol{H}}{\partial t}. \tag{3}$$

By substituting (2) into (3), the curl–curl equation of the total electric field in the time domain can be obtained

$$\nabla \times \nabla \times \boldsymbol{E} = -\mu_0 \frac{\partial (\sigma \boldsymbol{E} + J_s)}{\partial t}. \tag{4}$$

For a 3-D Earth model, the total electric field E can be expressed as the sum of the primary and secondary E-fields, and the actual conductivity σ can be expressed as the sum of the background and anomalous conductivities as follows:

$$\boldsymbol{E} = \boldsymbol{E_P} + \boldsymbol{E_S} \tag{5}$$

$$\sigma = \sigma_P + \sigma_S \tag{6}$$

where $\boldsymbol{E_P}$ denotes the primary electric field, $\boldsymbol{E_S}$ denotes the secondary electric field, σ_P denotes the background conductivity, and σ_S denotes the anomalous conductivity.

Equations (5) and (6) are substituted into (4) to yield

$$\nabla \times \nabla \times (\boldsymbol{E_P} + \boldsymbol{E_S}) = -\mu_0 \frac{\partial (\sigma_P + \sigma_S)(\boldsymbol{E_P} + \boldsymbol{E_S})}{\partial t} - \mu_0 \frac{\partial \boldsymbol{J_S}}{\partial t}. \tag{7}$$

Similar to (4), the curl–curl equation of the primary field can be expressed as

$$\nabla \times \nabla \times \boldsymbol{E_P} = -\mu_0 \frac{\partial \sigma_P \boldsymbol{E_P}}{\partial t} - \mu_0 \frac{\partial \boldsymbol{J_S}}{\partial t}. \tag{8}$$

Subtracting (8) from (7), the curl–curl equation of the secondary electric field is obtained

$$\nabla \times \nabla \times \boldsymbol{E_S} + \mu_0 \sigma \frac{\partial \boldsymbol{E_S}}{\partial t} = -\mu_0 \sigma_S \frac{\partial \boldsymbol{E_P}}{\partial t}. \tag{9}$$

Equation (9) is the final equation to be solved in this article. In (9), $\boldsymbol{E_P}$ is the primary electric field corresponding to the background model, which can be obtained by the analytical solution of the homogeneous half-space Earth model. $\boldsymbol{E_S}$ is the secondary electric field corresponding to the 3-D Earth model. Ultimately, the total electric field can be obtained by the sum of the solved secondary electric field and the primary electric field using (5), and the TEM response $\partial \mu_0 \boldsymbol{H}/\partial t$ can be calculated by the rotation of the total electric field using (1).

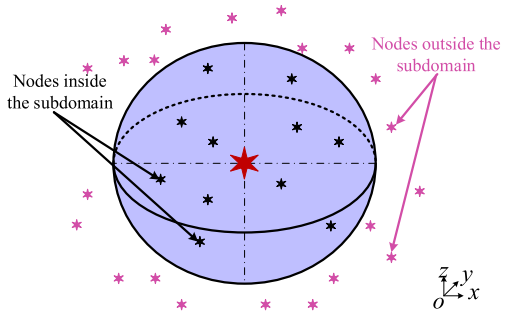

Fig. 2. Layout schematic of the 3-D GFDM point allocation.

III. Methodologies of the GFDM

According to the basic theory of the GFDM, which is based on the moving least squares method and the Taylor expansion, a point cloud (regular or irregularly distributed) in the computational domain should be first discretized by scattering arbitrary points in the solution domain [40], [41], [42], [43], [44], [45]. For each given central point (x_i, y_i, z_i), the nearest m points from the central point are found to form a subdomain within a specified distance d, as shown in Fig. 2.

Suppose that $s_i(x_i, y_i, z_i)$ is the function value of the central point (x_i, y_i, z_i), which is represented by the red star in Fig. 2, and $s_j^i (j = 1, 2, 3, \ldots, m)$ is the function value of the support points (x_j, y_j, z_j) within the point cluster, which are represented by the black stars in Fig. 2 (m is the total number of support points inside the subdomain). The second-order Taylor expansion at the central point (x_i, y_i, z_i) can be expressed by

$$\begin{aligned} s_j^i = s_i &+ h_{ij}\frac{\partial s_i}{\partial x} + k_{ij}\frac{\partial s_i}{\partial y} + l_{ij}\frac{\partial s_i}{\partial z} + \frac{h_{ij}^2}{2}\frac{\partial^2 s_i}{\partial x^2} \\ &+ \frac{k_{ij}^2}{2}\frac{\partial^2 s_i}{\partial y^2} + \frac{l_{ij}^2}{2}\frac{\partial^2 s_i}{\partial z^2} \\ &+ h_{ij}k_{ij}\frac{\partial^2 s_i}{\partial x \partial y} + h_{ij}l_{ij}\frac{\partial^2 s_i}{\partial x \partial z} + k_{ij}l_{ij}\frac{\partial^2 s_i}{\partial y \partial z} \\ &+ \boldsymbol{O}(\rho^2)(j = 1, 2, 3, \ldots, m) \end{aligned} \tag{10}$$

where $h_{ij} = x_j - x_i$, $k_{ij} = y_j - y_i$, $l_{ij} = z_j - z_i$, and $\rho = (h_{ij}^2 + h_{ij}^2 + l_{ij}^2)^{1/2}$.

The following residual function is defined using the moving least squares principle:

$$\begin{aligned} R(s) = \sum_{j=1}^{m} \Bigg[& s_i - s_j^i + h_{ij}\frac{\partial s_i}{\partial x} + k_{ij}\frac{\partial s_i}{\partial y} + l_{ij}\frac{\partial s_i}{\partial z} + \frac{h_{ij}^2}{2}\frac{\partial^2 s_i}{\partial x^2} \\ &+ \frac{k_{ij}^2}{2}\frac{\partial^2 s_i}{\partial y^2} + \frac{l_{ij}^2}{2}\frac{\partial^2 s_i}{\partial z^2} + h_{ij}k_{ij}\frac{\partial^2 s_i}{\partial x \partial y} \\ &+ h_{ij}l_{ij}\frac{\partial^2 s_i}{\partial x \partial z} + k_{ij}l_{ij}\frac{\partial^2 s_i}{\partial y \partial z} \Bigg]^2 \omega^2(d_{ij}) \end{aligned} \tag{11}$$

where $\omega(d_{ij})$, which is given by the following equation, denotes the weighting function of each support point and d_{ij} denotes the distance between the central point (x_i, y_i, z_i) and

the support point (x_j, y_j, z_j) [38]

$$\omega(d_{ij}) = \begin{cases} 1-6\left(\frac{d_{ij}}{d_m}\right)^2+8\left(\frac{d_{ij}}{d_m}\right)^3-3\left(\frac{d_{ij}}{d_m}\right)^4 & d_{ij} \le d_m \\ 0 & d_{ij} > d_m \end{cases} \tag{12}$$

where d_m denotes the distance between the central point (x_i, y_i, z_i) and the farthest support point within the point cluster.

To some extent, the weighting function reflects the influence of the function values at different support points on the function value at the central point; the closer the distance between the support point and the central point, the greater the value of the weighting function is.

Taking the minimal value of the residual function (11), the partial derivative of $R(s)$ with respect to each order partial derivative term $\boldsymbol{D_s}$ should be equal to zero

$$\frac{\partial R(s)}{\partial \boldsymbol{D}_s} = 0 \tag{13}$$

where

$$\boldsymbol{D}_s = \left\{ \frac{\partial s_i}{\partial x}, \frac{\partial s_i}{\partial y}, \frac{\partial s_i}{\partial z}, \frac{\partial^2 s_i}{\partial x^2}, \frac{\partial^2 s_i}{\partial y^2}, \frac{\partial^2 s_i}{\partial z^2}, \frac{\partial^2 s_i}{\partial x \partial y}, \frac{\partial^2 s_i}{\partial x \partial z}, \frac{\partial^2 s_i}{\partial y \partial z} \right\}^T.$$

Combining (10)–(13), the following equation can be obtained:

$$\boldsymbol{A}\boldsymbol{D}_s = \boldsymbol{b} \tag{14}$$

where $\boldsymbol{\varepsilon_{ij}} = \{h_{ij}, k_{ij}, l_{ij}, (h_{ij}^2/2), (k_{ij}^2/2), (l_{ij}^2/2), h_{ij}k_{ij}, k_{ij}l_{ij}, k_{ij}l_{ij}\}^T$, $\boldsymbol{A} = \sum_{j=1}^{m} \omega^2(d_{ij})\boldsymbol{\varepsilon_{ij}}\boldsymbol{\varepsilon_{ij}^T}$, and $b = \sum_{j=1}^{m} \omega^2(d_{ij})\varepsilon_{ij}(s_j^i - s_i)$.

By solving (14), the explicit expression for each order of partial derivative in $\boldsymbol{D}_s$ can be denoted as a linear combination of the function values of the support points and that of the central point

$$\begin{aligned} \boldsymbol{D}_s &= \boldsymbol{A}^{-1}\boldsymbol{b} = \boldsymbol{A}^{-1}\boldsymbol{b} = \boldsymbol{A}^{-1}\sum_{j=1}^{m} \omega^2(d_{ij})\boldsymbol{\varepsilon_{ij}}(s_j^i - s_i) \\ &= \boldsymbol{e_i}s_i + \sum_{j=1}^{m} \boldsymbol{e_j^i}s_j^i \end{aligned} \tag{15}$$

where $\boldsymbol{e_i} = -\sum_{j=1}^{m} \boldsymbol{A}^{-1}\varepsilon_{ij}\omega^2(d_{ij})$ and $\boldsymbol{e_j^i} = \boldsymbol{A}^{-1}\boldsymbol{\varepsilon_{ij}}\omega^2(d_{ij})$.

IV. Generalized Finite Difference Analysis of the Electromagnetic Problem

By replacing the partial derivative terms in (9) with the corresponding terms of the explicit expression of $\boldsymbol{D}_s$ in (15) and applying the discrete differential format for $(\partial \boldsymbol{E_S}/\partial t) = (s_i^{n+1} - s_i^n/\Delta t)$ and $(\partial \boldsymbol{E_P}/\partial t) = (p_i^{n+1} - p_i^n/\Delta t)$, the GFDM equations for the TEM problem are given as

$$\boldsymbol{ae_i}s_i + \sum_{j=1}^{m} \boldsymbol{ae_j^i}s_j^i + \mu_0\sigma\frac{s_i^{n+1} - s_i^n}{\Delta t} = -\mu_0\sigma_S\frac{p_i^{n+1} - p_i^n}{\Delta t} \tag{16}$$

where $\boldsymbol{a}$ is the introduced vector given by $\boldsymbol{a} = (0, 0, 0, 1, 1, 1, 0, 0, 0)$. s_i^n and s_i^{n+1} are the function values to be solved (i.e., the secondary electric field) for the central point at moments t^n and t^{n+1}, respectively. p_i^n and p_i^{n+1} are the known primary electric field values for the central point at moments t^n and t^{n+1}, respectively, which can be calculated by the analytical solution.

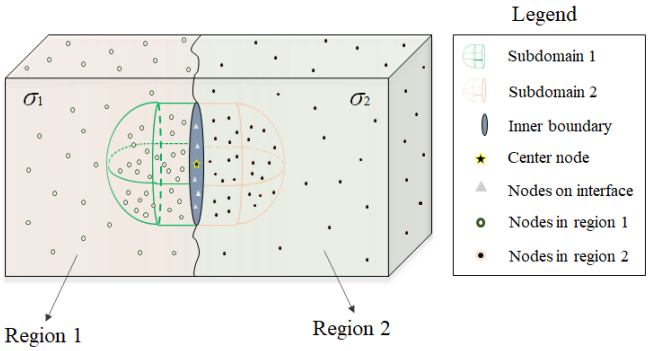

Fig. 3. Schematic of the two independent mesh-free subdomains (i.e., subdomains 1 and 2) at two sides of the interface. The conductivities for the points in regions 1 and 2 are recorded as σ_1 and σ_2, respectively.

By reorganizing, (16) can be rewritten in the iterative form as

$$s_i^{n+1} = s_i^n + \left(\boldsymbol{ae_i}s_i + \sum_{j=1}^{m} \boldsymbol{ae_j^i}s_j^i\right)\frac{\Delta t}{\mu_0\sigma} - \frac{\sigma_S}{\sigma}p_i^{n+1} + \frac{\sigma_S}{\sigma}p_i^n. \tag{17}$$

Considering all points inside the computational domain and those on the boundary, the following set of linear equation systems is obtained:

$$\boldsymbol{C}_{N\times N}\boldsymbol{x}_{N\times 1} = \boldsymbol{f}_{N\times 1} \tag{18}$$

where $\boldsymbol{C}$ is the final coefficient matrix with a dimension of $N \times N$ (N is the total number of unknowns in the computational domain), and it is a sparse matrix with at most $m + 1$ (m is much smaller than N) nonzero elements in each row. $\mathbf{x}$ is the function value vector to be solved. $\mathbf{f}$ is the right-hand side term, i.e., the source term, the value of which is known.

V. Boundary Conditions and Conductivity Assignment for Interface Points

A. Outer Boundary Conditions

A convenience of using the secondary electric field equation is that the secondary field on the outer boundary of the model (denoted by the symbol Γ) can be approximated as zero when the boundary is far enough away from the target study area. Based on this, the following outer boundary conditions, i.e., the Dirichlet boundary conditions, are used:

$$n \times \boldsymbol{E_s}\big|_{\Gamma} = 0. \tag{19}$$

B. Inner Interface Conditions and Conductivity Assignment for Interface Points

To ensure the discontinuity of the normal component of the E-field at interfaces, two independent mesh-free subdomains (subdomains 1 and 2), one each at the two sides of an

interface, are constructed. This means that the linear equation corresponding to the points on the interface should be deduced and derived twice: once for each subdomain. The conductivity of the points on the interface should also be assigned twice separately. At each assignment, the value of conductivity is set the same as that on the points inside the corresponding subdomain. A schematic of this concept is shown in Fig. 3. Although this results in an increased number of equations in the system to be solved (the increase in number depends on the number of points on the inner interfaces), it is an effective way to reproduce the discontinuous property. Using the above process, the discontinuity also imposes the tangential component of the E-fields and the normal current density, which is not expected. To solve this problem, the continuity conditions at interfaces are directly and enforcedly incorporated into the linear equation system by the following equations:

$$\boldsymbol{E}_T^1 = \boldsymbol{E}_T^2$$

and

$$\sigma^1 \boldsymbol{E}_N^1 = \sigma^2 \boldsymbol{E}_N^2$$

where $\boldsymbol{E}_T^1$ and $\boldsymbol{E}_T^2$ and $\boldsymbol{E}_N^1$ and $\boldsymbol{E}_N^2$ represent the tangential components of the E-field for subdomains 1 and 2 and the normal components of the E-field for subdomains 1 and 2, respectively; and σ^1 and σ^2 represent the conductivities of subdomains 1 and 2, respectively.

VI. Examples

To verify the correctness of the GFDM algorithm and the developed 3-D forward modeling program, two groups of typical 3-D Earth models, i.e., double-block land TEM models and topography semi-airborne TEM models, are considered. The TEM response (i.e., $d\boldsymbol{B}_z/dt$) of the above models is calculated using the developed GFDM program, and the results are compared with the equivalent responses computed using other methods.

As the 3-D forward modeling of the TEM responses based on the GFDM is carried out by adopting the secondary electric field equation, the prerequisite for an accurate simulation of the secondary electric field is the precise calculation of the primary electric field. In this article, the primary electric field is computed using a program developed on the MATLAB platform according to the analytical solution of a homogeneous Earth model [46]. To verify the correctness of the primary electric field [i.e., the source term in the right-hand term of (9) and (18)], the analytical solution of the TEM responses ($d\boldsymbol{B}_z/dt$) for the background model (i.e., the homogeneous half-space Earth model) of the 3-D Earth models considered in this article is first calculated and compared with the equivalent FEM numerical solution for the same model.

A. Verification of the Correctness of the Analytical Solution of the TEM Response for the Homogeneous Half-Space Earth Model

The parameters of the homogeneous half-space Earth model are set as follows: the conductivity is 0.01 S/m and the model size is 60 × 60 × 40 km ($x \times y \times z$). The wire source is placed along the x-direction, with a length of 1 km and a current of 40 A. The center of the source is located at the origin. A schematic of the configuration of the model is shown in Fig. 4.

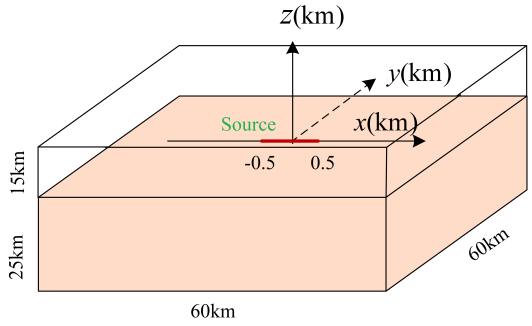

Fig. 4. Schematic of the homogeneous half-space model.

As the TEM response spreads downward with the extension of time and gradually decays with time, the TEM responses (i.e., $d\boldsymbol{B}_z/dt$) for different time channels can reflect the distribution of the underground resistivity at different depths. Based on this, the analytical solution of the model for four typical time channels, i.e., 10^{-4}, 10^{-3}, 10^{-2}, and 10^{-1}s, are considered; the responses at the ground surface are calculated, and they are compared with the equivalent FEM numerical solution for the same model. The results are shown in Fig. 5.

The reason for choosing $d\boldsymbol{B}_z/dt$ as the TEM response to be compared and analyzed in this example (as well as in the following 3-D Earth model example) is that the previous works in the literature showed that for the type of model configuration considered in this article, $d\boldsymbol{B}_z/dt$ can better indicate the underground abnormal bodies than the $d\boldsymbol{B}_x/dt$ and $d\boldsymbol{B}_y/dt$ responses. This is manifested in the larger value of the relative anomaly of the $d\boldsymbol{B}_z/dt$ responses (the relative anomaly is calculated from the ratio of the secondary-induced electromotive force to the total-induced electromotive force) [47].

By comparing the analytical solutions and the numerical FE solutions for the abovementioned four time channels shown in Fig. 5, it can be seen that the TEM responses (i.e., $d\boldsymbol{B}_z/dt$) for the homogeneous half-space Earth model calculated using the two methods coincide well with each other, which verifies the correctness of the computation of the primary TEM responses. It can also be observed that the amplitude of $d\boldsymbol{B}_z/dt$ gradually decays with the extension of the shutdown time, which is consistent with the physical properties of the TEM responses. This again verifies that the program is able to reproduce the varying characteristics of the primary TEM response. As the primary TEM response is calculated from the rotation of the primary electric field using (1), the correctness of the primary electric field (i.e., the source term) is naturally and indirectly verified.

B. Verification of the Correctness of the Numerical Solution of the Land TEM Response for the 3-D Double-Block Models

The three typical 3-D double-block models considered here are Model 1 with two conductive blocks, Model 2 with two

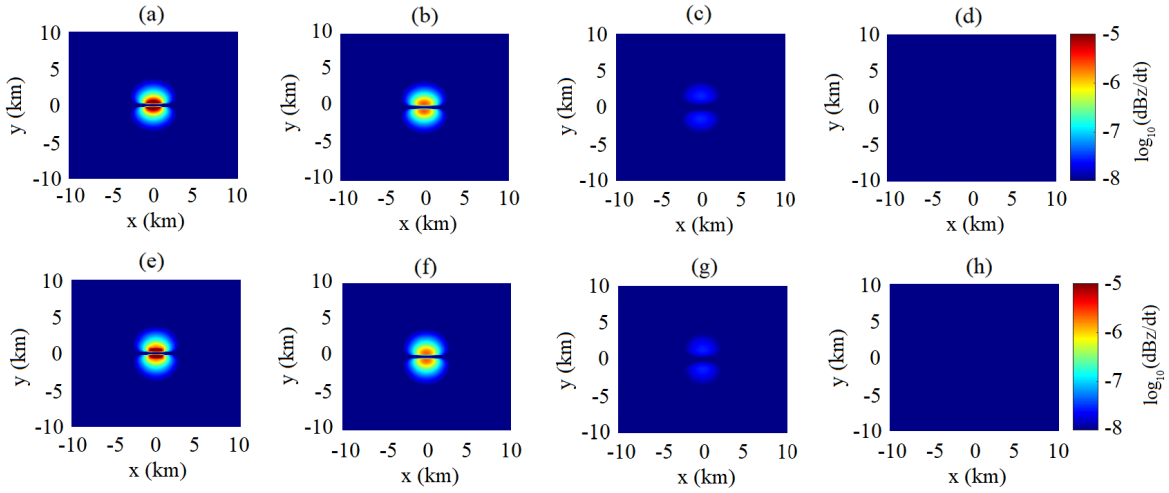

Fig. 5. Comparison between the analytical solution and the numerical FEM solution of the TEM response ($d\boldsymbol{B}_z/dt$) for the homogeneous half-space Earth model at the ground surface. (a)–(d) and (e)–(h) First and second rows represent the analytical solution and the numerical FEM solution for the homogeneous half-space Earth model, respectively. The first to fourth columns show the TEM response for the time channels of 10^{-4}, 10^{-3}, 10^{-2}, and 10^{-1} s, respectively. The color bar is applied to each row of the panels and indicates the value of $\log_{10} d\boldsymbol{B}_z/dt$. The logarithmic value of $d\boldsymbol{B}_z/dt$ is utilized because the magnitude of the TEM response varies greatly with spatial location, and it can span several orders of magnitude. This property makes it difficult to visualize the changing characteristics of the TEM response using a linear scale, so we show the responses on a logarithmic scale to better present the variation. The utilization of the logarithmic scale is also extended to Figs. 7, 9, 11, and 13.

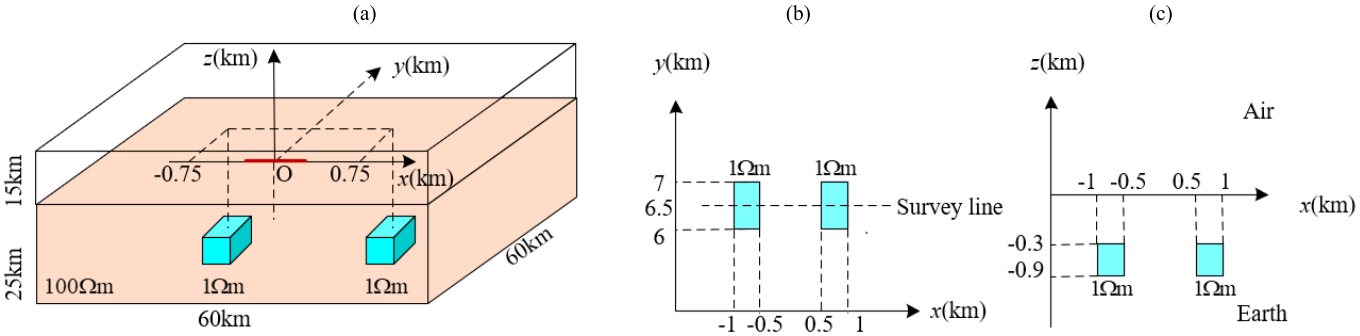

Fig. 6. Schematic of Model 1. (a) 3-D view of Model 1. (b) Plan view of Model 1. (c) Section view of Model 1. The red line in (a) represents the wire source.

resistive blocks, and Model 3 with one conductive and one resistive block. The parameters of Model 1 are given as follows: the resistivity of both blocks is 1 Ωm, their size is 500 × 1000 × 600 m ($x \times y \times z$), and the centers are located at (−750, 6500, −600 m) and (750, 6500, −600 m). All other parameters are the same as those of the homogeneous half-space Earth model shown in Fig. 4. The parameters of Models 2 and 3 are the same as those of Model 1 except for the resistivity of the blocks. In Model 2, the resistivity of both blocks is 10 000 Ωm. In Model 3, the resistivity of the conductive block is 1 Ωm, and that of the resistive block is 10 000 Ωm. The schematics of the 3-D double-block models are shown in Figs. 6, 8, and 10. To verify the correctness of the 3-D GFDM forward modeling algorithm and the accuracy of the computation of the developed program, the TEM response (i.e., $d\boldsymbol{B}_z/dt$) of the above three models is calculated using the developed GFDM program, and the results are compared with the equivalent responses computed using the FEM. The comparison of the responses computed using the two methods for the three models is shown in Figs. 7, 9, and 11. The TEM response of the homogeneous half-space Earth model is also shown in these figures for comparison to highlight the characteristics of the anomalous response caused by the abnormal body (i.e., the blocks).

The following three characteristics can be observed from the combined analysis of Figs. 7, 9, and 11.

First, the GFDM solution of the TEM response is highly consistent with the corresponding FEM solution for all three models. The average relative error and the maximum relative error between the two methods are 3.4% and 5.6%, respectively. The correctness of the proposed GFDM algorithm, the accuracy of the computation of the developed program, and the availability of their application in the 3-D forward modeling of the TEM response are therefore verified.

Second, by comparing the TEM response of the 3-D double-block model and that of the homogeneous half-space Earth model correspondingly, it can be seen that the response near the resistive and conductive blocks shows positive and negative anomalies, respectively. The locations of the anomalies reflected by the response are consistent with the actual

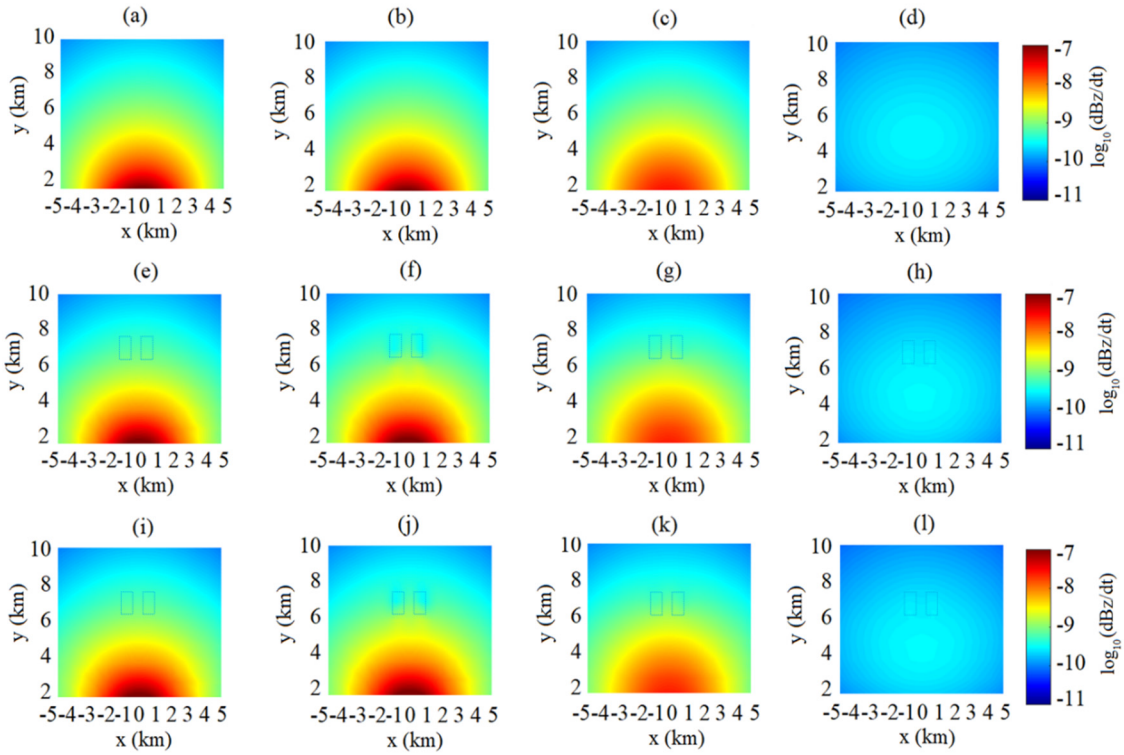

Fig. 7. Comparison of the GFDM and FEM solutions of the TEM response ($d\boldsymbol{B}_z/dt$) in the $z = 0$ plane for Model 1. (a)–(d) First row shows the analytical solution of the homogeneous half-space Earth model. (e)–(h) and (i)–(l) Second and third rows show the GFDM solution and the FEM solution of Model 1, respectively. The first to fourth columns show the responses for the time channels 10^{-4}, 10^{-3}, 10^{-2}, and 10^{-1} s, respectively. The blue dashed rectangular box represents the actual location of the two conductive blocks in Model 1. The color bar is applied to each row of the panels and indicates the value of $\log_{10}(d\boldsymbol{B}_z/dt)$.

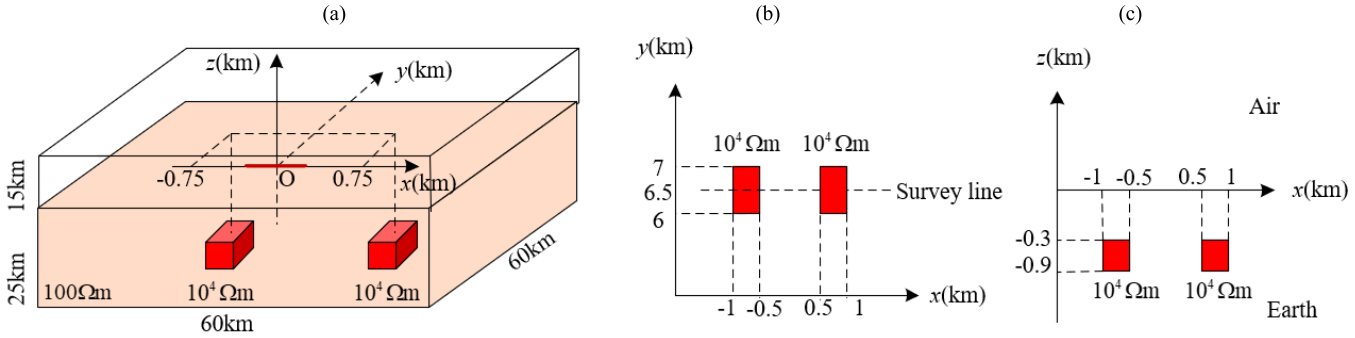

Fig. 8. Schematic of Model 2. (a) 3-D view of Model 2. (b) Plan view of Model 2. (c) Section view of Model 2. The red line in (a) represents the wire source.

locations of the anomalies in the given model. Furthermore, by comparing the anomalous response of the conductive and resistive blocks, it can be seen that the TEM response is more sensitive to conductive anomalies. These characteristics all coincide with the property of the TEM response.

Third, by comparing the responses of different time channels for each model, the existence of anomalies cannot be effectively reflected by the response of the time channel 10^{-4} s, but the responses of time channels 10^{-3}, 10^{-2}, and 10^{-1} s can clearly indicate the existence of the anomalies and accurately suggest their location and property (i.e., conductive or resistive). This is because the anomalies in the considered models are buried relatively deeply, and the survey points are arranged in a relatively long distance from the source. According to the smoke ring theory, the TEM response spreads downward and far away with the extension of time. At an early time (i.e., 10^{-4} s), the response has not yet spread to the lateral location and depth of the anomalies, so the response does not contain the anomalous response caused by the anomalies. With the continuous extension of time, the response spreads further and deeper. When it arrives at the location that covers the anomalies, the anomaly caused by the anomalies would be contained in the measured responses, which is the reason why the positive and negative anomalies in the area where the anomaly is located can be clearly seen in the TEM response of the other three time channels (i.e., later time). The above results further demonstrate that the GFDM algorithm proposed and the program developed in this article can accurately, stably, and effectively reproduce the characteristics of the 3-D TEM responses of different time channels and different locations.

We also investigate the property of the coefficient matrix of the GFDM, and the positions of the nonzero elements of the

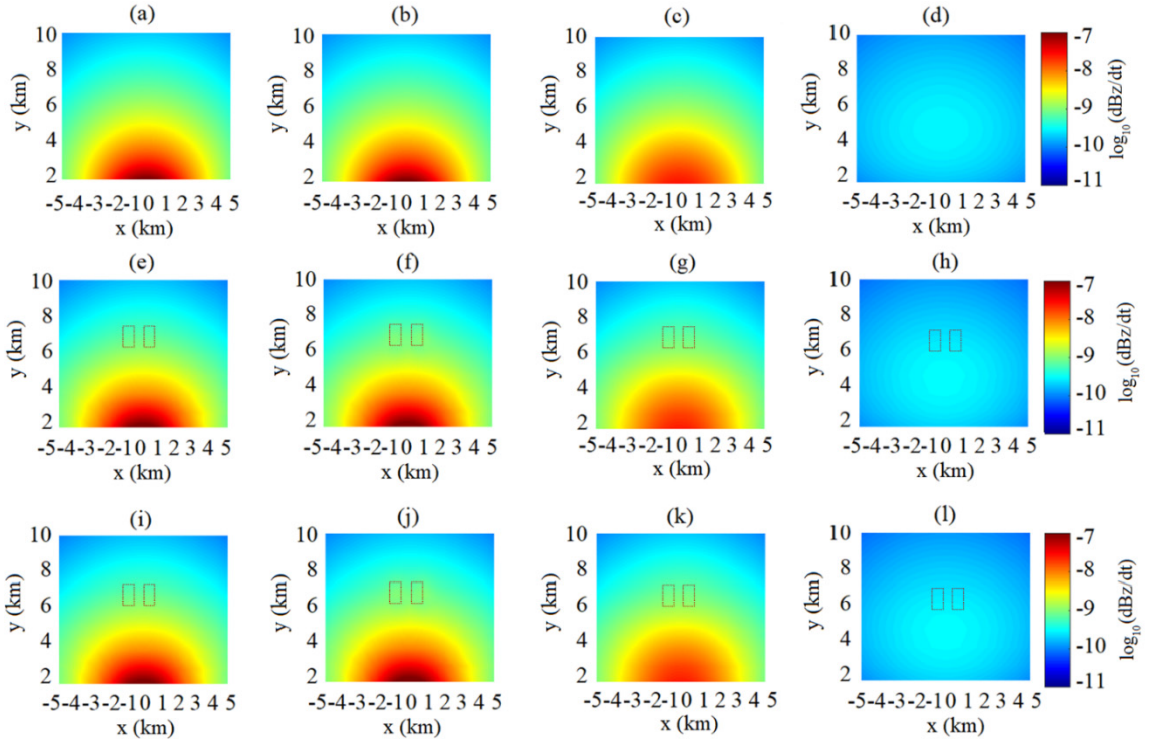

Fig. 9. Comparison of the GFDM and FEM solutions of the TEM response ($d\boldsymbol{B}_z/dt$) in the $z = 0$ plane for Model 2. (a)–(d) Analytical solution of the homogeneous half-space Earth model. (e)–(h) GFDM solution and (i)–(l) FEM solution of Model 2, respectively. The first to fourth columns show the responses for the time channels 10^{-4}, 10^{-3}, 10^{-2}, and 10^{-1} s, respectively. The red dashed rectangular box represents the actual location of the two resistive blocks in Model 2. The color bar is applied to each row of the panels and indicates the value of $\log_{10}(d\boldsymbol{B}_z/dt)$.

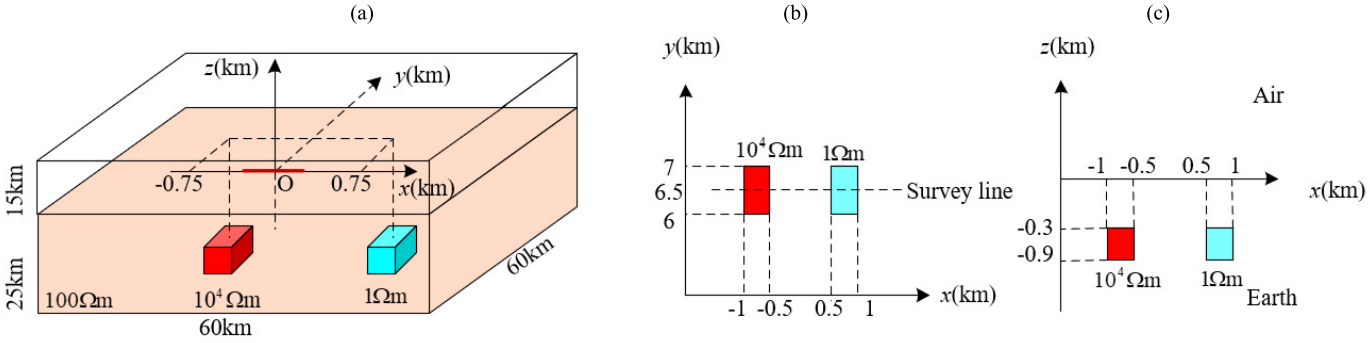

Fig. 10. Schematic of Model 3. (a) 3-D view of Model 3. (b) Plan view of Model 3. (c) Section view of Model 3. The red line in (a) represents the wire source.

coefficient matrix of the GFDM and the FEM are shown in Fig. 12. The computation speed and memory consumption of the GFDM are also evaluated by comparing these parameters with those of the FEM. To enhance the comparability, the positions of the discretized points for the GFDM in this article are the same as the positions of the vertices of the mesh generated for the FEM. Under such a discretization strategy, it was found that the total number of nonzero elements of the coefficient matrix of the GFDM is significantly less than that of the FEM. Correspondingly, the computation speed is higher, and the memory requirement is lower. In particular, taking the computational parameters of Model 1 (for the time channel of 10^{-4} s) as an example, the total number of nonzero elements of the coefficient matrix of the GFDM, which is derived from the discretization considered here and the weighting function, is 690 876. The corresponding computation time is 67.45 s, and the memory consumption is 11.56 GB. In comparison, the total number of nonzero elements of the coefficient matrix of the FEM, which is derived from the same discretization but considering the integral of the production of the function and the edge basis functions, is 1 401 476. The corresponding computation time is 99.31 s, and the memory consumption is 14.56 GB. The above results illustrate that under comparable computational accuracy, the GFDM possesses advantages in terms of computational time and memory consumption. Such advantages will be more prominent in the forward modeling of responses of more complex models (e.g., models with complex topography or targets with complex shapes).

The above forward modeling and comparison mainly focus on the analysis of the lateral distribution characteristics of

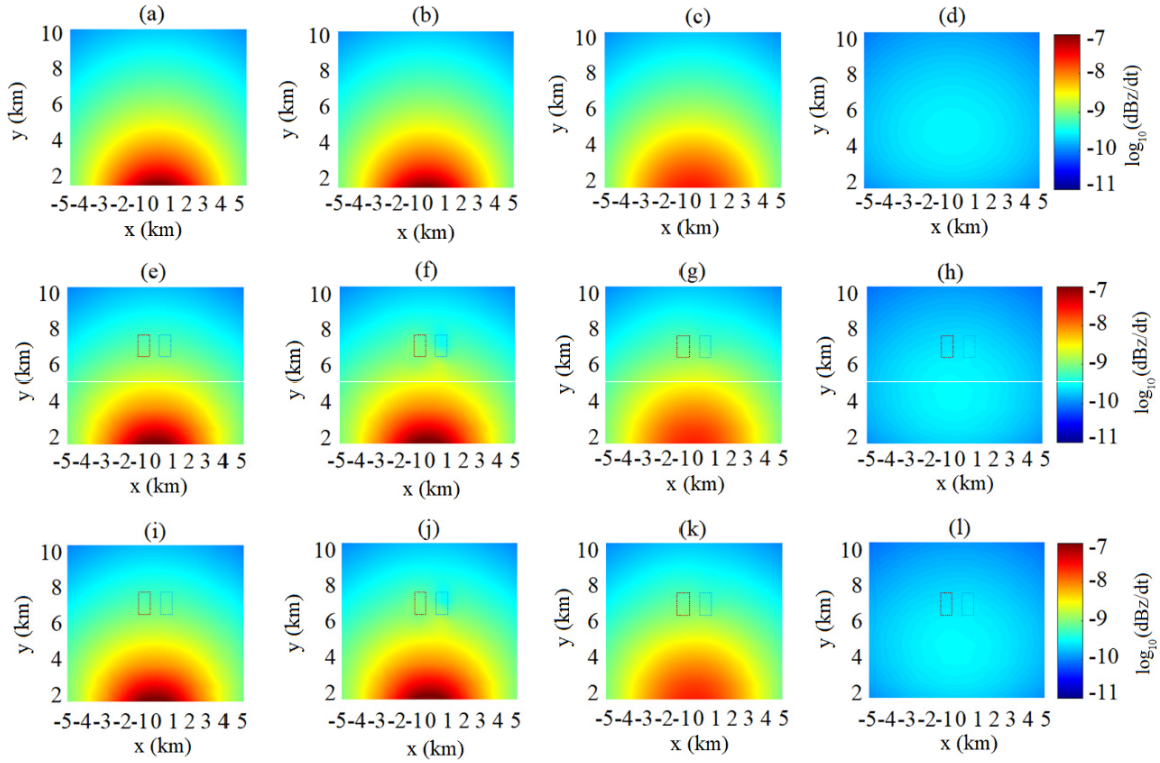

Fig. 11. Comparison of the GFDM and FEM solutions of the TEM response ($d\boldsymbol{B}_z/dt$) in the $z = 0$ plane for Model 3. (a)–(d) Analytical solution of the homogeneous half-space Earth model. (e)–(h) GFDM solution and (i)–(l) FEM solution of Model 3, respectively. The first to fourth columns show the responses for the time channels 10^{-4}, 10^{-3}, 10^{-2}, and 10^{-1} s, respectively. The blue and red dashed rectangular box represents the actual location of the conductive and the resistive block in Model 3, respectively. The color bar is applied to each row of the panels and indicates the value of $\log_{10}(d\boldsymbol{B}_z/dt)$.

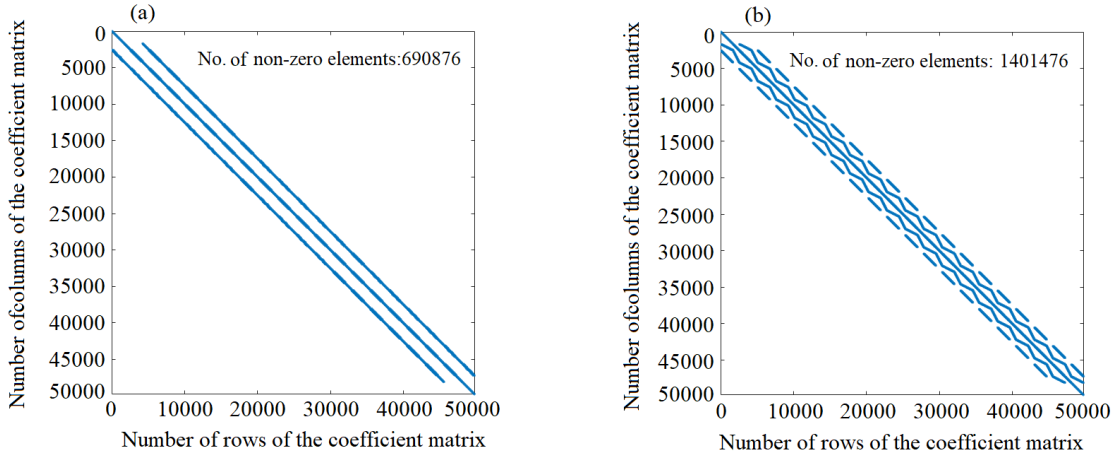

Fig. 12. Schematic of the positions of the nonzero elements in the coefficient matrix of (a) GFDM and (b) FEM. The x-axis and y-axis coordinates of the blue dots represent the number of rows and columns of the nonzero elements in the coefficient matrix.

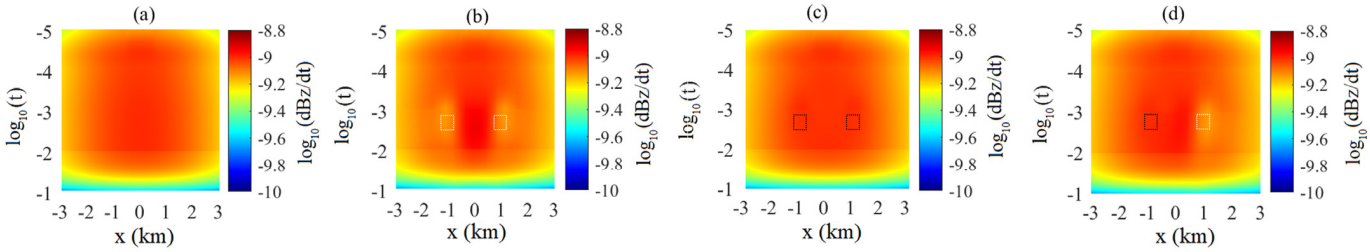

Fig. 13. Pseudo-sections of the TEM response along the line $y = 6500$ m at the ground surface. (a)–(d) TEM response of the homogeneous half-space Earth model, Model 1, Model 2, and Model 3, respectively. The black and white dashed rectangular boxes represent the resistive and conductive blocks, respectively.

the TEM response at the ground surface. To more comprehensively analyze various characteristics of the response with time, the TEM response of numerous 400 time channels (a time range varying from 10^{-5} to 10^{-1} s, which is uniformly distributed in log space, is considered) along the line $y = 6500$ m (which is located directly above the center

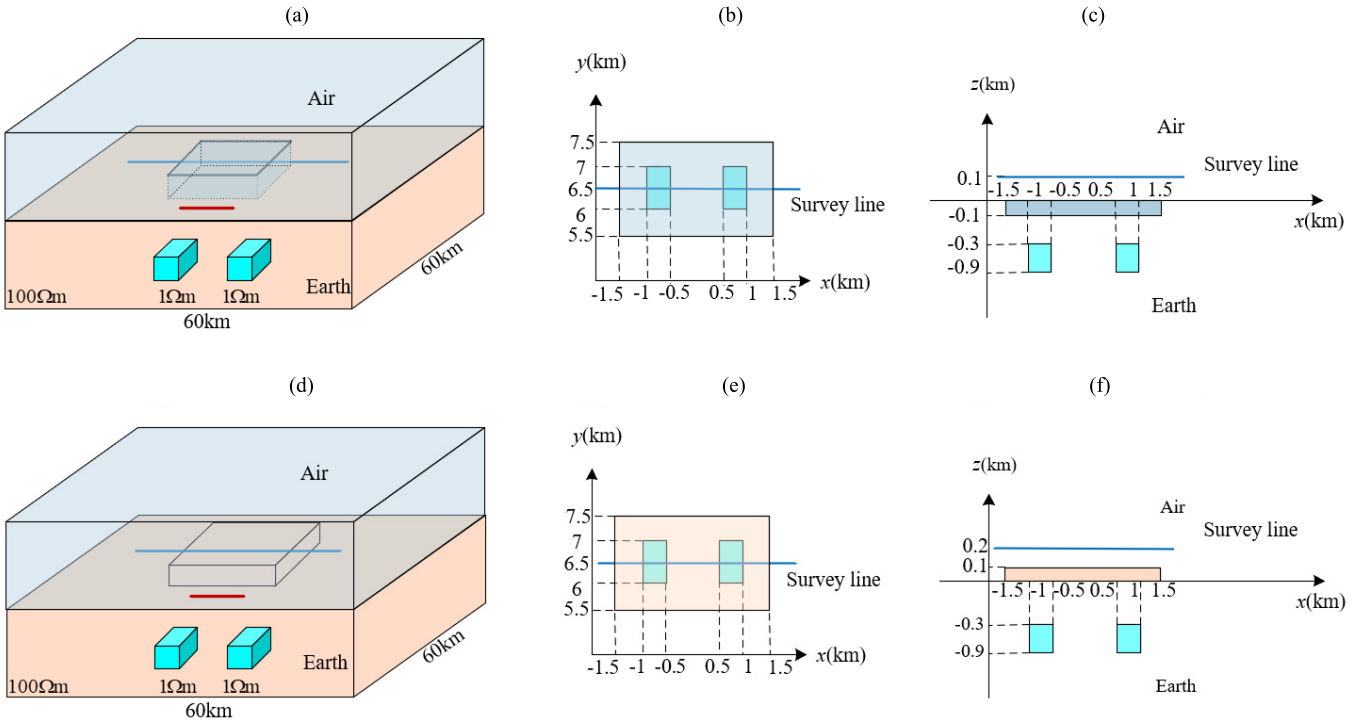

Fig. 14. Schematic of Models 4 and 5. (a) 3-D view of Model 4. (b) Plan view of Model 4. (c) Section view of Model 4. (d) 3-D view of Model 5. (e) Plan view of Model 5. (f) Section view of Model 5. The red line in (a) and (d) represents the wire source.

of the anomaly at the ground surface) is calculated, and pseudo-sections are drawn. The results are shown in Fig. 13. Since the time t corresponds to the diffusion depth z according to smoke ring theory, the xt plane can also be understood as the xz plane, i.e., the longitudinal plane; hence, such a figure can also be used to analyze various characteristics of the response with the longitudinal position of anomalies (i.e., depth).

In Fig. 13, it can be seen that in the spatial dimension (i.e., the x-axis), the anomalous position coincides with the horizontal position where the actual anomalous body is in the given model. In the time dimension (i.e., the t-axis), the anomalies presented are more concentrated and obvious in the time range of 10^{-3}–10^{-2} s. According to the smoke ring theory, the diffusion depth corresponding to the above time range is consistent with the longitudinal position of the actual anomalies in the given model. This verifies that the TEM response calculated by the GFDM method proposed in this article can not only reveal the property and the horizontal position of the anomalies but also accurately indicate their longitudinal position through the responses of different time channels.

C. Verification of the Correctness of the Numerical Solution of the Semi-Airborne TEM Response for 3-D Models With Both Topography and Targets

To verify the correctness of the numerical solution of the TEM response for more complex models, we considered a semi-airborne model (i.e., Model 4) with concave topography and a model (i.e., Model 5) with convex topography. The diagrams of Models 4 and 5 are shown in Fig. 14. The parameters of the topography are given as follows: the resistivity of the convex topography is set to 100 Ωm, the resistivity of the concave topography is set to 10^8 Ωm, the size of both is (3000, 2000, 100 m), and the centers are located at (0, 6500, 50 m) and (0, 6500, −50 m). The parameters of the targets and the parameters of the source in Models 4 and 5 are set the same as those in Model 1. The TEM response of Model 4 on the $z = 100$ m observation plane and that of Model 5 on the $z = 200$ m plane are calculated using the GFDM, and the results are compared with the equivalent FEM solutions. The comparison of the responses is shown in Fig. 15. The responses computed using the two methods show good agreement with each other. This verifies the feasibility and accuracy of the GFDM algorithm and program on the application of modeling the TEM response of more complex Earth models.

In addition, by comparing the TEM response of Models 4 and 5 with that of Model 1, it can be found that the response value near the convex topography shows a decreasing tendency, and the response value near the concave topography shows an increasing tendency. This verifies the ability of the GFDM algorithm and program to reproduce the anomaly caused by the topography. In addition, by comparing the TEM response of different time channels, it is seen that the anomaly caused by the topography, both concave and convex, is more obvious at early times than at late times. This is because the early time response contains more information on abnormal bodies at shallow depths, and the convex and concave topographies can be treated as shallow conductive abnormal bodies extending from the surface upward to the air and resistive abnormal bodies downward to the underground, respectively. This indicates that the late-time TEM response is more capable of mitigating the effect of topography.

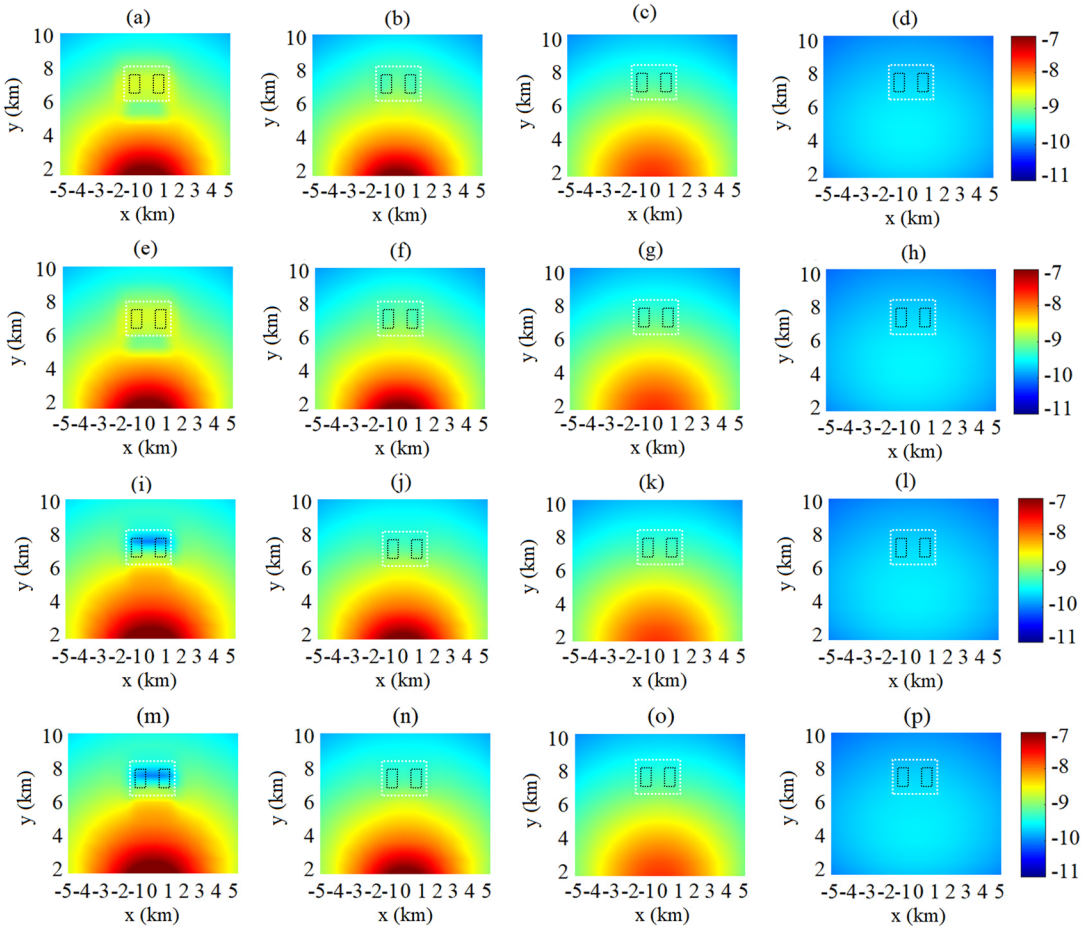

Fig. 15. Comparison of the GFDM and FEM solutions of the semi-airborne TEM response ($d\boldsymbol{B}_z/dt$) on the $z = 100$ m plane for Model 4 and on the $z = 200$ m plane for Model 5. (a)–(d) and (e)–(h) First and second rows show the GFDM solution and the FEM solution of Model 4, respectively. (i)–(l) and (m)–(p) Third and fourth rows show the GFDM solution and the FEM solution of Model 5, respectively. The first to fourth columns show the responses for the time channels 10^{-4}, 10^{-3}, 10^{-2}, and 10^{-1} s, respectively. The white and black dashed rectangular boxes represent the actual locations of the topography and the targets in Models 4 and 5, respectively. The color bar is applied to each row of the panels and indicates the value of $\log_{10}(d\boldsymbol{B}_z/dt)$.

VII. Conclusion

The 3-D forward modeling of ground wire source TEM data based on the GFDM is proposed in this article, and a corresponding program is developed on the MATLAB platform. One of the main features of the GFDM that differs from the FEM in the forward modeling process is that mesh generation is not needed; instead, the computational region is discretized by a point cloud, which allows the points to distribute freely to fit the arbitrary shape of the complex models, which is helpful in ensuring the computational accuracy of the simulation of the TEM responses for realistic 3-D Earth models. In addition, as the basis function and integral are not needed in the GFDM as they are in the FEM, this simplifies the overall procedure of the forward modeling, improves computational efficiency and reduces memory consumption. This is fully illustrated in the comparison of the computational parameters (i.e., the positions and numbers of nonzero elements in the coefficient matrix, the computation time, and the memory consumption) of the GFDM and the FEM.

The abovementioned features are a major advantage of the GFDM method. However, these features also lead to a problem: unlike the FEM, the source term on the right-hand side of the linear equation system, which contains the derivative of the pseudo-δ function with respect to time, is spatially integrated inside the local element of the mesh, and such an integral results in a constant value (i.e., the product of the length of the wire source and current flowing through it) according to the property of the pseudo-δ function. However, in the GFDM, this kind of source term equivalence cannot be applied directly in the forward modeling of the GFDM, because without the integral, handling the source term in this way would result in an infinite value, which cannot be handled numerically. In this article, this problem is solved by deriving a secondary field equation for the GFDM, which replaces the source term with the time derivative of the primary electric field (which can be easily calculated by the analytical solution) of the background Earth model (homogenous half-space Earth model) to avoid using the pseudo-δ function and confronting an infinite value.

The secondary field linear equation system of the GFDM determines that the accurate simulation of the primary electric field (i.e., the source term) at any point inside the computational domain is a prerequisite for the accurate calculation

of the TEM response. Therefore, we first program a code to calculate the analytical solution of the primary electric field of a homogeneous half-space Earth model and compare the analytical solution with the equivalent numerical FEM solution. The consistency of the two results verifies the accuracy of the source term. On this basis, several 3-D models are considered, and the TEM responses of these models are calculated using the developed GFDM program. By comparing the forward modeling results of the GFDM with those of the FEM, it is verified that the GFDM algorithm proposed herein can accurately compute the TEM response of 3-D models with higher efficiency and lower memory requirements. Thus, the effectiveness and advantages of the proposed GFDM algorithm and the developed program are demonstrated. In future work, the application of the GFDM to the forward modeling of TEM data for more realistic and complex Earth models will be investigated.

ACKNOWLEDGMENT

The authors would like to thank Prof. Ruijie Ma from the College of Mathematics, Jilin University, for her assistance on some mathematical issues during the research.

REFERENCES

[1] J. Chang, J. Yu, J. Li, G. Xue, R. Malekian, and B. Su, "Diffusion law of whole-space transient electromagnetic field generated by the underground magnetic source and its application," *IEEE Access*, vol. 7, pp. 63415–63425, 2019, doi: 10.1109/ACCESS.2019.2916767.

[2] F. Liu et al., "Reducing motion-induced noise with mechanically resonant coil sensor in a rigid helicopter transient electromagnetic system," *IEEE Trans. Ind. Electron.*, vol. 67, no. 3, pp. 2391–2401, Mar. 2020, doi: 10.1109/TIE.2019.2907495.

[3] B. Su, J. Yu, G. M. Królczyk, P. Gardoni, and Z. Li, "Innovative surface-borehole transient electromagnetic method for sensing the coal seam roof grouting effect," *IEEE Trans. Geosci. Remote Sens.*, vol. 60, 2022, Art. no. 5702509, doi: 10.1109/TGRS.2022.3149212.

[4] M. A. Vallée, R. S. Smith, and P. Keating, "Case history of combined airborne time-domain electromagnetics and power-line field survey in Chibougamau, Canada," *Geophysics*, vol. 75, no. 2, pp. 67–72, Mar. 2010, doi: 10.1190/1.3343573.

[5] J. E. Danielsen, E. Auken, F. Jørgensen, V. Søndergaard, and K. I. Sørensen, "The application of the transient electromagnetic method in hydrogeophysical surveys," *J. Appl. Geophys.*, vol. 53, no. 4, pp. 181–198, Oct. 2003, doi: 10.1016/j.jappgeo.2003.08.004.

[6] S. Malecki, R.-U. Börner, and K. Spitzer, "A new method for absolute underground positioning based on transient electromagnetics," *Geophys. J. Int.*, vol. 221, no. 1, pp. 87–96, Apr. 2020, doi: 10.1093/gji/ggz540.

[7] Z. Jiang, L. Liu, S. Liu, and J. Yue, "Surface-to-underground transient electromagnetic detection of water-bearing goaves," *IEEE Trans. Geosci. Remote Sens.*, vol. 57, no. 8, pp. 5303–5318, Aug. 2019, doi: 10.1109/TGRS.2019.2898904.

[8] L. Song, S. D. Billings, L. R. Pasion, and D. W. Oldenburg, "Transient electromagnetic scattering of a metallic object buried in underwater sediments," *IEEE Trans. Geosci. Remote Sens.*, vol. 54, no. 2, pp. 1091–1102, Feb. 2016, doi: 10.1109/TGRS.2015.2473851.

[9] F. L. Teixeira and W. C. Chew, "Finite-difference computation of transient electromagnetic waves for cylindrical geometries in complex media," *IEEE Trans. Geosci. Remote Sens.*, vol. 38, no. 4, pp. 1530–1543, Jul. 2000, doi: 10.1109/36.851953.

[10] J. Chang, X. Wu, K. Lei, P. Lv, Y. Zhao, and Q. Meng, "Three-dimensional modeling of ground-airborne transient electromagnetic responses of typical models based on the finite difference approach," *J. Appl. Geophys.*, vol. 197, Feb. 2022, Art. no. 104545, doi: 10.1016/j.jappgeo.2022.104545.

[11] C.-T. Hwang and R.-B. Wu, "Treating late-time instability of hybrid finite-element/finite-difference time-domain method," *IEEE Trans. Antennas Propag.*, vol. 47, no. 2, pp. 227–232, Feb. 1999, doi: 10.1109/8.761061.

[12] B. M. Gunderson, G. A. Newman, and G. W. Hohmann, "Three-dimensional transient electromagnetic responses for a grounded source," *Geophysics*, vol. 51, no. 11, pp. 2117–2130, Nov. 1986, doi: 10.1190/1.1442064.

[13] W. A. SanFilipo and G. W. Hohmann, "Integral equation solution for the transient electromagnetic response of a three-dimensional body in a conductive half-space," *Geophysics*, vol. 50, no. 5, pp. 798–809, May 1985, doi: 10.1190/1.1441954.

[14] G. A. Newman, G. W. Hohmann, and W. L. Anderson, "Transient electromagnetic response of a three-dimensional body in a layered earth," *Geophysics*, vol. 51, no. 8, pp. 1608–1627, Aug. 1986, doi: 10.1190/1.1442212.

[15] T. Wang and G. W. Hohmann, "A finite-difference, time-domain solution for three-dimensional electromagnetic modeling," *Geophysics*, vol. 58, no. 6, pp. 797–809, Jun. 1993, doi: 10.1190/1.1443465.

[16] K. Yee, "Numerical solution of initial boundary value problems involving Maxwell's equations in isotropic media," *IEEE Trans. Antennas Propag.*, vol. AP-14, no. 3, pp. 302–307, May 1966, doi: 10.1109/TAP.1966.1138693.

[17] H. Jahandari and C. G. Farquharson, "Finite-volume modelling of geophysical electromagnetic data on unstructured grids using potentials," *Geophys. J. Int.*, vol. 202, no. 3, pp. 1859–1876, Jul. 2015, doi: 10.1093/gji/ggv257.

[18] J. Li, C. G. Farquharson, and X. Hu, "3D vector finite-element electromagnetic forward modeling for large loop sources using a total-field algorithm and unstructured tetrahedral grids," *Geophysics*, vol. 82, no. 1, pp. 1–16, Jan. 2017, doi: 10.1190/geo2016-0004.1.

[19] X. S. Lu and C. G. Farquharson, "3D finite-volume time-domain modeling of geophysical electromagnetic data on unstructured grids using potentials," *Geophysics*, vol. 85, pp. 221–240, Nov. 2020, doi: 10.1190/geo2020-0088.1.

[20] H. Jahandari, S. Ansari, and C. G. Farquharson, "Comparison between staggered grid finite-volume and edge-based finite-element modelling of geophysical electromagnetic data on unstructured grids," *J. Appl. Geophys.*, vol. 138, pp. 185–197, Mar. 2017, doi: 10.1016/j.jappgeo.2017.01.016.

[21] H. Si, "TetGen, a delaunay-based quality tetrahedral mesh generator," *ACM Trans. Math. Softw.*, vol. 41, no. 2, pp. 1–36, Feb. 2015, doi: 10.1145/2629697.

[22] P. G. Lelièvre et al., "FacetModeller: Software for manual creation, manipulation and analysis of 3D surface-based models," *SoftwareX*, vol. 7, pp. 41–46, Jan. 2018, doi: 10.1016/j.softx.2018.02.002.

[23] P. Lelièvre, A. Carter-McAuslan, C. Farquharson, and C. Hurich, "Unified geophysical and geological 3D Earth models," *Lead. Edge*, vol. 31, no. 3, pp. 322–328, Mar. 2012, doi: 10.1190/1.3694900.

[24] H. Jahandari and C. G. Farquharson, "A finite-volume solution to the geophysical electromagnetic forward problem using unstructured grids," *Geophysics*, vol. 79, pp. 287–302, Nov. 2014, doi: 10.1190/geo2013-0312.1.

[25] E. A. Badea, M. E. Everett, G. A. Newman, and O. Biro, "Finite-element analysis of controlled-source electromagnetic induction using Coulomb-gauged potentials," *Geophysics*, vol. 66, no. 3, pp. 786–799, May 2001, doi: 10.1190/1.1444968.

[26] J. Long and C. G. Farquharson, "On the forward modelling of three-dimensional magnetotelluric data using a radial-basis-function-based mesh-free method," *Geophys. J. Int.*, vol. 219, no. 1, pp. 394–416, Oct. 2019, doi: 10.1093/gji/ggz306.

[27] M. Zhang, C. G. Farquharson, and C. S. Liu, "2.5-D forward modeling of the frequency-domain ground-airborne electromagnetic response in areas with topographic relief," *Chin. J. Geophys.*, vol. 64, no. 1, pp. 327–342, 2021, doi: 10.6038/cjg2020N0182.

[28] S. Ansari and C. G. Farquharson, "3D finite-element forward modeling of electromagnetic data using vector and scalar potentials and unstructured grids," *Geophysics*, vol. 79, no. 4, pp. 149–165, Jul. 2014, doi: 10.1190/geo2013-0172.1.

[29] Y. Chung, J.-S. Son, T. J. Lee, H. J. Kim, and C. Shin, "Three-dimensional modelling of controlled-source electromagnetic surveys using an edge finite-element method with a direct solver," *Geophys. Prospecting*, vol. 62, no. 6, pp. 1468–1483, Nov. 2014, doi: 10.1111/1365-2478.12132.

[30] M. Zhang, C. G. Farquharson, and T. Lin, "Comparison of nodal and edge basis functions for the forward modelling of three-dimensional frequency-domain wire source electromagnetic data using a potentials formulation," *Geophys. Prospecting*, vol. 70, no. 4, pp. 828–843, May 2022, doi: 10.1111/1365-2478.13187.

[31] M. Zhang, C. G. Farquharson, and T. Lin, "Three-dimensional forward modeling and characterization of the responses of the ground-airborne frequency-domain electromagnetic method," *J. Appl. Geophys.*, vol. 199, Apr. 2022, Art. no. 104588, doi: 10.1016/j.jappgeo.2022.104588.

[32] Y. H. Chen, W. C. Chew, and M. L. Oristaglio, "Application of perfectly matched layers to the transient modeling of subsurface EM problems," *Geophysics*, vol. 62, no. 6, pp. 1730–1736, Nov. 1997.

[33] G. Li, Y. Li, B. Han, and Z. Liu, "Application of the perfectly matched layer in 3-D marine controlled-source electromagnetic modelling," *Geophys. J. Int.*, vol. 212, no. 1, pp. 333–344, Jan. 2018, doi: 10.1093/gji/ggx382.

[34] S. D. L. K. de Ryhove and R. Mittet, "3D marine magnetotelluric modeling and inversion with the finite-difference time-domain method," *Geophysics*, vol. 79, no. 6, pp. 269–286, Nov. 2014, doi: 10.1190/geo2014-0110.1.

[35] G. Li, L. Zhang, and B. K. Goswami, "Complex frequency-shifted perfectly matched layers for 2.5D frequency-domain marine controlled-source EM field simulations," *Surveys Geophys.*, vol. 43, no. 4, pp. 1055–1084, Aug. 2022, doi: 10.1007/s10712-022-09699-z.

[36] Y. Hu, G. Egbert, Y. Ji, and G. Fang, "A novel CFS-PML boundary condition for transient electromagnetic simulation using a fictitious wave domain method," *Radio Sci.*, vol. 52, no. 1, pp. 118–131, Jan. 2017, doi: 10.1002/2016RS006160.

[37] R. Schaback, "Convergence of unsymmetric kernel-based meshless collocation methods," *SIAM J. Numer. Anal.*, vol. 45, no. 1, pp. 333–351, Jan. 2007, doi: 10.1137/050633366.

[38] Y. Ji, T. Huang, W. Huang, and L. Rong, "Meshfree method in geophysical electromagnetic prospecting: The 2D magnetotelluric example," *Int. J. Comput. Methods*, vol. 15, no. 2, Mar. 2018, Art. no. 1750084, doi: 10.1142/S0219876217500840.

[39] J. Wittke and B. Tezkan, "Meshfree magnetotelluric modelling," *Geophys. J. Int.*, vol. 198, no. 2, pp. 1255–1268, May 2014, doi: 10.1093/gji/ggu207.

[40] J. Chen, Y. Gu, M. Wang, W. Chen, and L. Liu, "Application of the generalized finite difference method to three-dimensional transient electromagnetic problems," *Eng. Anal. Boundary Elements*, vol. 92, pp. 257–266, Jul. 2018, doi: 10.1016/j.enganabound.2017.08.015.

[41] L. Gavete, M. L. Gavete, and J. J. Benito, "Improvements of generalized finite difference method and comparison with other meshless method," *Appl. Math. Model*, vol. 27, no. 10, pp. 831–847, 2003, doi: 10.1016/S0307-904X(03)00091-X.

[42] J. J. Benito, F. Urena, L. Gavete, and R. Alvarez, "An h-adaptive method in the generalized finite differences," *Comput. Methods Appl. Mech. Eng.*, vol. 192, pp. 735–759, 2003, doi: 10.1016/S0045-7825(02)00594-7.

[43] F. Ureña, L. Gavete, A. García, J. J. Benito, and A. M. Vargas, "Solving second order non-linear parabolic PDEs using generalized finite difference method (GFDM)," *J. Comput. Appl. Math.*, vol. 354, pp. 221–241, Jul. 2019, doi: 10.1016/j.cam.2018.02.016.

[44] W. Zhan, X. Rao, H. Zhao, H. Zhang, S. Hu, and W. Dai, "Generalized finite difference method (GFDM) based analysis for subsurface flow problems in anisotropic formation," *Eng. Anal. Boundary Elements*, vol. 140, pp. 48–58, Jul. 2022, doi: 10.1016/j.enganabound.2022.04.008.

[45] A. Kamyabi, V. Kermani, and M. Kamyabi, "Improvements to the meshless generalized finite difference method," *Eng. Anal. Boundary Elements*, vol. 99, pp. 233–243, Feb. 2019, doi: 10.1016/j.enganabound.2018.11.002.

[46] S. H. Ward and G. W. Hohmann, "Electromagnetic theory for geophysical applications," in *Electromagnetic Methods in Applied Geophysics*, M. N. Nabighian, Ed., 3rd ed. Tulsa, OK, USA: Society of Exploration Geophysicist, 1988, pp. 130–311, doi: 10.1190/1.9781560802631.ch4.

[47] Y. J. Ji, Y. Q. Wu, S. S. Guan, and X. J. Zhao, "3D numerical modeling of induced-polarization electromagnetic response based on the finite-difference time-domain method," *Geophysics*, vol. 83, pp. 385–389, Nov. 2018, doi: 10.1190/geo2017-0190.1.

Tianjiao Li was born in Changchun, China, in 1989. He received the B.S. and M.S. degrees from Jilin University, Changchun, China, in 2012 and 2015, respectively. He is currently pursuing the Ph.D. degree with the University of Chinese Academy of Sciences, Beijing, China, and Jilin University.

His research interests include the forward modeling of geophysical electromagnetic data and remote sensing technology.

Ming Zhang was born in Changchun, China, in 1989. She received the B.S., M.S., and Ph.D. degrees from Jilin University, Changchun, China, in 2011, 2014, and 2020, respectively.

From 2018 to 2020, she was with the Memorial University of Newfoundland, St. John's, NL, Canada, as a Visiting Graduate Student. She is currently a Post-Doctoral Fellow at Jilin University. Her research interests include forward modeling and inversion of geophysical electromagnetic data.

Jun Lin received the B.S. and M.S. degrees in applied geophysics from the Changchun College of Geosciences, Changchun, China, in 1982 and 1987, respectively.

In 1989, he was a Visiting Scholar with the University of Leicester, Leicester, U.K. In 1996, he was a Senior Scholar with the University of Arizona, Tucson, AZ, USA. Since 2005, he has been the Chairperson with the College of Instrumentation and Electrical Engineering, Jilin University, Changchun. He is currently a Professor with Jilin University. He has finished 13 national projects. He has authored ten books, more than 300 articles, and 50 patents. His research interests include seismic instruments, nuclear magnetic resonance instruments, and time- and frequency-domain electromagnetic instrument developments, as well as geophysical modeling processes.

Mr. Lin was a recipient of the two Key National Invention Awards as the Chief Director.